Geophysical Research Letters

RESEARCH LETTER
10.1029/2020GL087775

Key Points:
- Distribution of interseismic coupling on the North and East Anatolian Faults
- Bayesian quantification of uncertainties on coupling and Euler poles
- The 2020 M_w 6.8 Elazig earthquake released 221.5 years (±26) of accumulated moment

Supporting Information:
- Supporting Information S1

Correspondence to:
Q. Bletery,
bletery@geoazur.unice.fr

Citation:
Bletery, Q., Cavalié, O., Nocquet, J. M., & Ragon, T. (2020). Distribution of interseismic coupling along the North and East Anatolian Faults inferred from InSAR and GPS data. *Geophysical Research Letters*, *47*, e2020GL087775. https://doi.org/10.1029/2020GL087775

Received 4 MAR 2020
Accepted 5 AUG 2020
Accepted article online 17 AUG 2020

Distribution of Interseismic Coupling Along the North and East Anatolian Faults Inferred From InSAR and GPS Data

Quentin Bletery[1], Olivier Cavalié[1], Jean-Mathieu Nocquet[1,2], and Théa Ragon[3]

[1]Université Côte d'Azur, IRD, CNRS, Observatoire de la Côte d'Azur, Géoazur, France, [2]Institut de Physique du Globe de Paris, Université de Paris, CNRS, Paris, France, [3]Seismological Laboratory, California Institute of Technology, Pasadena, CA, USA

Abstract The North Anatolian Fault (NAF) has produced numerous major earthquakes. After decades of quiescence, the M_w 6.8 Elazığ earthquake (24 January 2020) has recently reminded us that the East Anatolian Fault (EAF) is also capable of producing significant earthquakes. To better estimate the seismic hazard associated with these two faults, we jointly invert interferometric synthetic aperture radar (InSAR) and GPS data to image the spatial distribution of interseismic coupling along the eastern part of both the NAF and EAF. We perform the inversion in a Bayesian framework, enabling to estimate uncertainties on both long-term relative plate motion and coupling. We find that coupling is high and deep (0–20 km) on the NAF and heterogeneous and superficial (0–5 km) on the EAF. Our model predicts that the Elazığ earthquake released between 200 and 250 years of accumulated moment, suggesting a bicentennial recurrence time.

Plain Language Summary Earthquakes are thought to occur on coupled fault portions, which are "locked" during the time separating two earthquakes, while tectonic plates are steadily moving. The spatial distribution of coupling has been imaged along numerous large faults in the world, but despite its considerable associated seismic hazard, not on the North Anatolian Fault (NAF). The recent M_w 6.8 Elazığ earthquake (24 January 2020) has reminded us that the East Anatolian Fault (EAF) is also capable of producing large earthquakes. To better assess the seismic hazard associated with both the NAF and the EAF, we image the distribution of interseismic coupling along these faults. We find that the NAF is strongly coupled along most of the studied section. On the opposite, coupling is shallow and heterogeneous along the EAF. The initiation of the Elazığ earthquake coincides with a strongly locked but narrow (5 × 14 km) and superficial patch. The rest of the rupture extends over moderately coupled fault portions. We estimate that it took between 200 and 250 years to accumulate the moment released by the Elazığ event. Several fault segments along the EAF present similar coupling distributions, suggesting that, provided enough time, they could host earthquakes of similar magnitude.

1. Introduction

Earthquakes are thought to rupture fault portions that have previously accumulated a deficit of slip over tens to thousands of years (e.g., Avouac, 2015). Quantifying the spatial distribution of interseismic coupling—that is, the percentage of slip deficit with respect to the long-term drift of tectonic plates—along large faults is therefore crucial to anticipate earthquakes and better assess seismic hazard (e.g., Kaneko et al., 2010). The emergence of space geodetic techniques has allowed to infer interseismic coupling along a number of large faults during long quiescent periods of time separating one large earthquake to the next (e.g., Bürgmann et al., 2005; Jolivet et al., 2015; Loveless & Meade, 2011; Metois et al., 2016; Moreno et al., 2010; Nocquet et al., 2017; Protti et al., 2014). Though interseismic coupling models have been proposed to estimate the locking depth of the North Anatolian Fault (NAF) and East Anatolian Fault (EAF) (e.g., Aktug et al., 2013, 2016; Cavalié & Jónsson, 2014; Mahmoud et al., 2013; Tatar et al., 2012), none have quantified the lateral variations of coupling along these faults, which has limited the possibilities to study the spatial relationship between coupling and large earthquakes. The density of interferometric synthetic aperture radar (InSAR) observations (Cavalié & Jónsson, 2014) combined with sparser GPS measurements allows to infer these lateral variations of coupling on the eastern part of the NAF-EAF system (Figure 1).

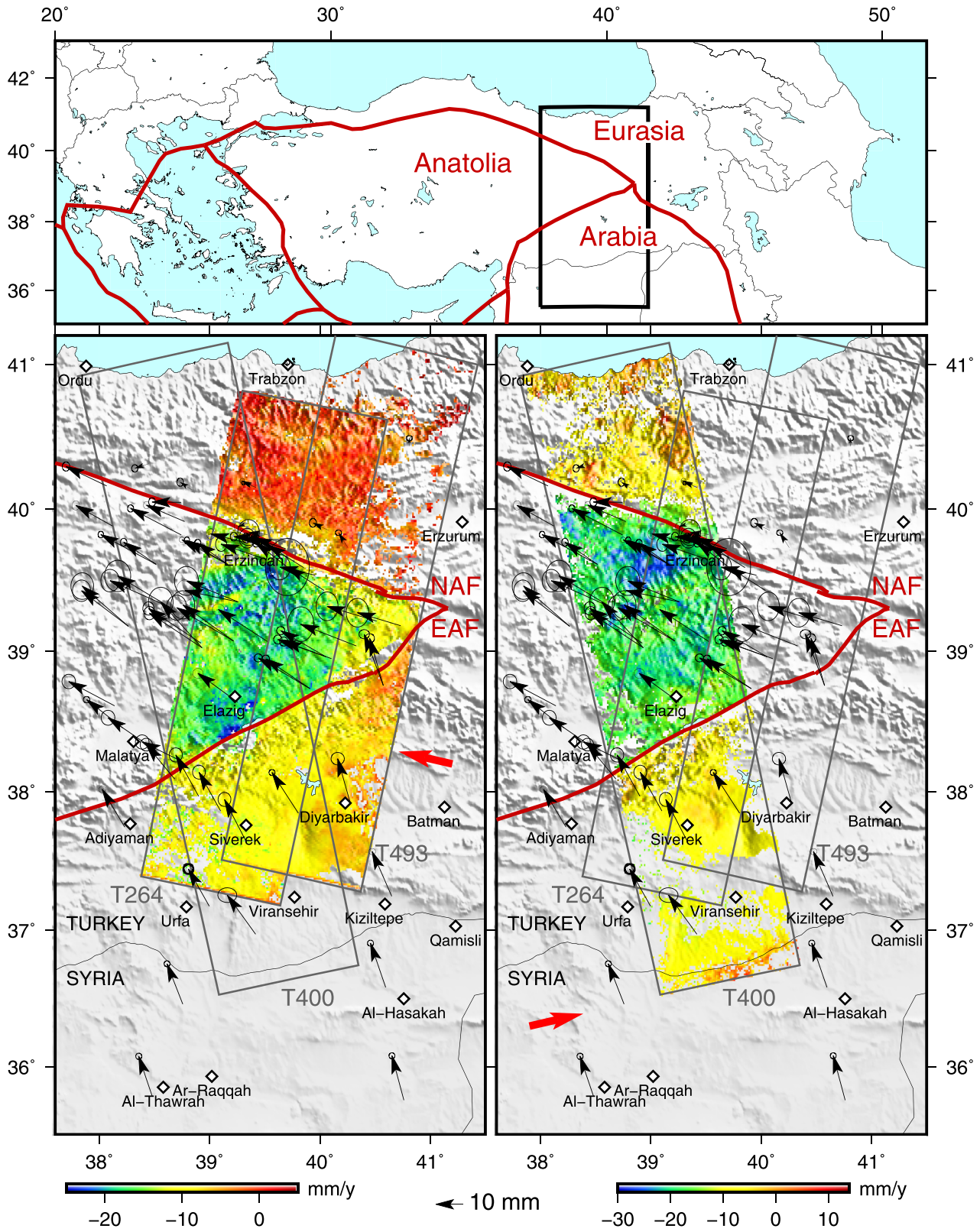

Figure 1. (top) Tectonic setting of the NAF-EAF system (red lines) and study area (black rectangle). (bottom) Color maps show InSAR horizontal velocities (in a Eurasiafixed reference frame) in the satellite line-of-sight (LOS) direction (thick red arrows), ~103°N for Descending Tracks T264 and T493 (left) and ~77°N for Ascending Track T400 (right) (Cavalié & Jónsson, 2014). Black arrows show GPS measurements and their 95% ellipses of uncertainty (Nocquet, 2012; Ozener et al., 2010; Tatar et al., 2012). White diamonds indicate large (>100,000 people) cities.

The eastern part of the NAF is known to produce large earthquakes (e.g., Ambraseys, 1971, 1989; Barka, 1996) and thought to be coupled from 0 to 15 km depth (Cavalié & Jónsson, 2014; Reilinger et al., 2006). On the other hand, simple back slip models showed that the EAF is weakly coupled and only in the first kilometers of the upper crust, from 0 to 5 km (Cavalié & Jónsson, 2014). This observation was in good agreement with the relative scarcity of large earthquakes recorded during the twentieth century (Burton et al., 1984; Jackson & McKenzie, 1988). For those reasons, the 24 January 2020 M_w 6.8 Elazığ earthquake came as a surprise, on a segment that does not exhibit signs of past rupture (Duman & Emre, 2013) and in an area where the last earthquake of comparable magnitude (M_S 6.8) occurred in 1905 (Nalbant et al., 2002). To understand this unexpected event, and more generally the seismicity in the region, we infer here the spatial distribution of interseismic coupling along the eastern part of the NAF-EAF system using InSAR (Cavalié & Jónsson, 2014) and GPS measurements (Nocquet, 2012; Ozener et al., 2010; Tatar et al., 2012) of the interseismic surface deformation.

Inferring spatially variable interseismic coupling along faults from geodetic observations—such as InSAR and GPS—of the Earth surface deformation requires solving an inverse problem that usually does not admit a unique solution (Nocquet, 2018; Tarantola & Valette, 1982). Most inversion techniques deal with this nonuniqueness by finding the solution that best fits the observations in a least squares sense, together with some roughness and/or damping penalty function. As a result, typical published coupling (or slip) models are the smoothest best fitting solutions among an infinity of possible models. We adopt here a Bayesian approach, which does not invert for a specific "ambiguously defined best solution" but explores the entire solution space, sampled with respect to the likelihood of each model. This approach—originally developed to invert for coseismic slip models (Minson et al., 2013)—also enables to reliably estimate uncertainties on coupling distributions (Jolivet et al., 2015, 2020).

2. Data

Our data set is composed of InSAR and GPS measurements in eastern Anatolia, all calculated in a stable Eurasia reference frame (Figure 1). Our InSAR data set is composed of two descending and one ascending tracks—all crossing both the NAF and EAF near their junction in eastern Turkey—processed by Cavalié and Jónsson (2014). Our GPS data set is composed of the horizontal components of 72 GPS stations located in the area (Nocquet, 2012; Ozener et al., 2010; Tatar et al., 2012).

InSAR data were derived from multiframe Envisat synthetic aperture radar (SAR) images provided by the European Space Agency. Each track includes between 16 and 19 SAR images acquired between 2003 and 2010. Interferograms were generated using the New Small BAseline Subset (NSBAS) processing chain (Doin et al., 2011). They were corrected for a ramp mostly due to a drift in the local oscillator on board the Envisat satellite (Marinkovic & Larsen, 2013). To avoid removing tectonic signals related to the motion of the Anatolian and Arabian plates, the ramps were estimated only on their Eurasian part that is considered as stable and orthogonal to the flight direction. All calculations were made considering stable Eurasia as a reference by setting the mean displacement of this area to 0, in the least squares sense. Surface displacement rates from the interferograms were derived using a small baseline time series approach, which maximizes coherence and the number of pixels to use in the analysis. A smoothing operator was applied to limit phase variations due to turbulent atmospheric delays. Finally, the linear component of the time series was extracted for each pixel in order to obtain the steady ground velocities. For a more detailed description of the InSAR processing, we refer the reader to the original study of Cavalié and Jónsson (2014).

Additionally, we compiled GPS data located between longitudes 38°E and 41°E and latitudes 35°N and 43°N from three independent studies. Velocity for 19 points were published by Tatar et al. (2012) derived from three surveys performed between 2006 and 2008. Another set of 19 points were published by Ozener et al. (2010) from three campaigns with 12-month interval. The remaining 34 points were originally published by Reilinger et al. (2006) and Reilinger and McClusky (2011) but recalculated in the continental-scale combination solution described in Nocquet (2012). The three data sets are expressed in a Eurasia-fixed reference frame. The lack of enough common sites shared among the three solutions prevents to properly combine them, but the few common sites and analysis of models residuals do not show any systematic pattern, suggesting that the three velocity fields are consistent within their uncertainties.

3. Bayesian Inversion of Rotation Poles and Interseismic Slip Deficit Rate Along Two Faults From InSAR and GPS Data

We invert the aforementioned InSAR and GPS measurements of the eastern Anatolia surface deformation to infer the distribution of interseismic slip deficit rate along the NAF-EAF system using a Bayesian sampling approach implemented in the AlTar1 package, originally developed by Minson et al. (2013) under the name of CATMIP. AlTar associates Markov chain Monte Carlo methods with a tempering process to explore the solution space, each step of the tempering being followed by a resampling to select only the most probable models. The probability density function (pdf) $p(\mathbf{m}|\mathbf{d})$ of a large number of likely models $\mathbf{m}$ given our data $\mathbf{d}$ is evaluated based on the ability of a model $\mathbf{m}$ to predict the data $\mathbf{d}$ (Minson et al., 2013):

$$p(\mathbf{m}|\mathbf{d}) \propto p(\mathbf{m}) \exp\left[-\frac{1}{2}(\mathbf{d}-\mathbf{G}\mathbf{m})^T \mathbf{C}_\chi^{-1}(\mathbf{d}-\mathbf{G}\mathbf{m})\right], \quad (1)$$

where $\mathbf{G}$ is the matrix of the Green's functions and $\mathbf{C}_\chi$ is the misfit covariance matrix. Vector $\mathbf{d}$ is composed of 144 GPS measurements (72×2 components) and a subset of InSAR pixels on the three tracks downsampled using the Quadtree algorithm (Jónsson et al., 2002).

Because the inferred distribution of coupling is presumably highly sensitive to the (usually) predetermined tectonic block motion, especially in a case involving three plates, we do not impose precalculated plate rotations but invert for them simultaneously with the interseismic slip deficit rate—similarly to the approach proposed by Meade and Loveless (2009) but adapted to a Bayesian framework. We discretize the eastern part of the NAF and EAF into 110 subfaults of depth-dependent sizes (Tables S1 and S2 in the supporting information) and invert for the model vector:

$$\mathbf{m} = \begin{pmatrix} \mathbf{w}^1 \\ \mathbf{w}^2 \\ \mathbf{S} \end{pmatrix}, \quad (2)$$

where $\mathbf{w}$ is the plate rotation vector expressed in Cartesian geocentric coordinates with unit of rad/year,[1] stands for Anatolia with respect to Eurasia,[2] for Arabia with respect to Eurasia, and $\mathbf{S}$ is the back slip on each subfault. Accordingly, we build $\mathbf{G}$ so that

$$\mathbf{G} = \left(\mathbf{A}, -\mathbf{G}_S\right), \quad (3)$$

where $\mathbf{A}$ is the matrix relating the plate rotation vectors to the horizontal velocities (see Appendix A) and $\mathbf{G}_S$ is the classical matrix of the Green's functions computed using the analytical solution of a shear finite fault embedded in an elastic half-space (Mansinha & Smylie, 1971; Okada, 1985).

$\mathbf{C}_\chi$ is the misfit covariance matrix, which translates data and epistemic uncertainties into uncertainties on the inverted model $\mathbf{m}$ (Bletery et al., 2016; Duputel et al., 2014; Ragon et al., 2018, 2019a, 2019b). Here, we only account for data uncertainties. For GPS records, we fill $\mathbf{C}_\chi$ with the (squared) standard deviations and covariances between the east and north components of a given station provided in the GPS solutions. For InSAR pixels, we first remove the tectonic signal from the unsampled interferograms using a preliminary model and calculate the covariance across the pixels of the residual interferograms as a function of their distances. We fit an exponential function (Figure S1) to the obtained cloud of points and express the covariance $C_{i,j}$ between two pixels as a function of their distance $D_{i,j}$:

$$C_{i,j} = a^2 \exp\left(\frac{-D_{i,j}}{b}\right), \quad (4)$$

by applying a regression to the parameters a and b independently on the three tracks (Jolivet et al., 2012, 2015, Sudhaus & Sigurjón, 2009). We then use Equation 4 to evaluate the covariance on the subsampled interferograms.

$p(\mathbf{m})$ is the pdf describing the prior information assumed on the different model parameters. We choose the less informative distributions for back slip parameters $\mathbf{S}$, that is, uniform distributions between 0 and the a priori long-term interplate velocities: 19.5 mm/year for the North Anatolian and 13 mm/year for the EAF (Cavalié & Jónsson, 2014). For the plate rotation vectors, we use the Euler poles and their associated

Table 1
A Priori (Le Pichon & Kreemer, 2010) and A Posteriori Euler Pole Coordinates and Angular Velocities With Respect to Eurasia

	Plate	Longitude (° E)	Latitude (° N)	Angular velocity (°/My)
A priori	Anatolia	31.96 ± 0.10	32.02 ± 0.10	1.307 ± 0.083
	Arabia	15.21 ± 0.10	28.31 ± 0.10	0.396 ± 0.010
A posteriori	Anatolia	34.22 ± 0.35	30.96 ± 0.60	1.087 ± 0.078
	Arabia	16.13 ± 0.52	27.08 ± 0.37	0.386 ± 0.008

Note. A posteriori parameters are the mean and 2-σ standard deviation (95% confidence) of the posterior pdfs (Figure S6).

uncertainty from Le Pichon and Kreemer (2010) to derive a prior pdf. Plate rotation vectors (in Cartesian geocentric coordinates) $\mathbf{w}^p$ are related to Euler pole parameters through

$$\mathbf{w}^p = \Omega^p \begin{pmatrix} \cos\phi^p \cos\lambda^p \\ \cos\phi^p \sin\lambda^p \\ \sin\phi^p \end{pmatrix}, \tag{5}$$

where λ^p and ϕ^p are the longitude and latitude of the Euler pole of a plate p and Ω^p is its angular velocity (Bowring, 1985). Note that this change of coordinate system makes the problem linear (e.g., Maurer & Johnson, 2014; Meade & Loveless, 2009; Nocquet et al., 2001). We draw 100,000 sets of parameters (λ^1, ϕ^1, Ω^1, λ^2, ϕ^2, Ω^2) from normal distributions defined by means and standard deviations taken from previously published solutions (Le Pichon & Kreemer, 2010, summarized in Table 1). For each drawn set of parameters, we calculate the corresponding $\mathbf{w}^1$ and $\mathbf{w}^2$. We obtain Gaussian-like distributions for each component of $\mathbf{w}^1$ (Figure S2) and $\mathbf{w}^2$ (Figure S3). We extract the mean and standard deviation of these distributions and use them to define normal prior pdfs on $w^{1,2}_{x,y,z}$ in AlTar.

4. Results

We obtain a posterior marginal pdf for every inverted parameter in $\mathbf{m}$, 110 fault slip parameters and 6 parameters describing the plate rotation vectors ($w^{1,2}_{x,y,z}$). The posterior pdfs on $\mathbf{w}^1$ and $\mathbf{w}^2$ parameters (Figure S4) appear uncorrelated (coefficients of correlation <0.013) with each other and—to a lesser extent—with fault slip parameters (coefficients of correlation <0.13) (Figure S5). Moderate anticorrelations are noticeable between fault slip parameters of patches located one beneath another (i.e., at the same location but different depth) (Figure S5a).

We convert the inverted pdfs on the rotation vectors ($\mathbf{w}^1$, $\mathbf{w}^2$) (Figure S4) into pdfs on the Euler pole coordinates and angular velocities (Figure S6). The means and 2-σ standard deviations of the inverted pdfs are summarized in Table 1. They are close to the previously published values we used as a prior (Le Pichon & Kreemer, 2010) but not equal (Figure S7). A possible explanation for this small discrepancy is that the plates are not strictly rigid (Aktug et al., 2013; England et al., 2016; Le Pichon & Kreemer, 2010; Nocquet, 2012), and thus, the rotations we invert from data in eastern Anatolia are slightly different from those obtained from data sampling on a larger area of the plate. Figure S8a shows the velocities corrected from plate motion using the Euler poles from Le Pichon and Kreemer (2010). It clearly shows a pattern of a residual rotation and unlikely large (5 mm/year) fault normal relative motion across both faults. Using our poles, residuals velocities appear to be consistent with the interseismic pattern (back slip) expected for strike-slip faults (Figure S8b). Our goal here is to infer the coupling distribution, and for that aim a refined estimate of the rotation parameters close to the fault is preferable to a plate-average solution, but one should be careful in using values in Table 1 for other purposes.

For each posterior Euler pole, we calculate the rotation predicted at the center of each patch and project the obtained vector along the fault strike direction to obtain posterior pdfs of the long-term slip rate along the faults (Figure S9). These pdfs are consistent with steady long-term slip rates of ~20 mm/year along the NAF and ~10 mm/year along the EAF (Figures 2 and S9 and Tables S1 and S2).

For each sampled model $\mathbf{m}_k = (\mathbf{w}^1_k, \mathbf{w}^2_k, \mathbf{S}_k)^T$, we divide the back slip parameters $\mathbf{S}_k$ by the long-term fault rate calculated at the center of each patch using the corresponding sampled Euler poles $\mathbf{w}^1_k$ and $\mathbf{w}^2_k$ to obtain

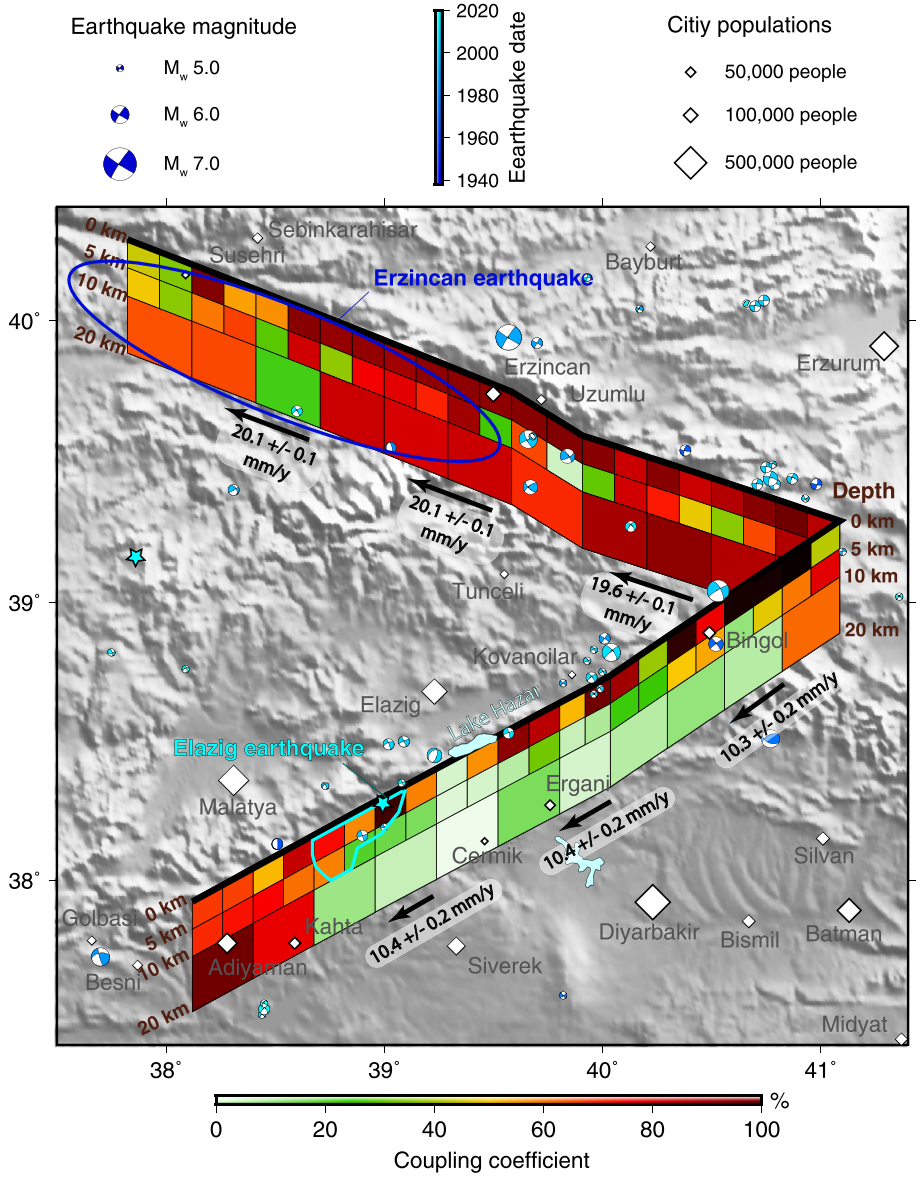

Figure 2. Interseismic coupling distribution inverted from InSAR and GPS data (mean of posterior pdfs in Figures S10 and S11). Black thick arrows indicate the long-term slip rate at depth derived from the inversion (mean and standard deviation of posterior pdfs in Figure S9). Focal mechanisms show $M > 4.8$ earthquakes (colors indicate event dates). Contours delineate the approximate rupture extent of the 1939 M_S 8.0 Erzincan earthquake and of the 2020 M_w 6.8 Elazığ earthquake (USGS finite fault solution). The light blue star indicates the epicenter of the Elazığ earthquake.

the posterior marginal pdfs on the coupling coefficients (Figures S10 and S11). We show these pdfs in the form of their means (Figure 2) and standard deviations (Figure 3). Although restrictive, this representation gives an approximate view of the coupling spatial distribution and its associated uncertainties. Uncertainty is high (>25%) on the extreme west and—to a lesser extent—the extreme east parts of the fault system that are located outside of the InSAR tracks (Figure 1). The standard deviation on most parts of the faults is <20%, much lower on many subfaults (Figure 3). Note that standard deviation values are likely underestimated since we did not consider epistemic uncertainties here. The Earth structure is likely not homogeneous and the fault geometry not as simple as we modeled it, generating more uncertainties that we do not account for.

We calculate the GPS and InSAR measurements predicted for every posterior sampled model. We plot the predicted GPS means (red arrows) and 2-σ standard deviations (red ellipses) on Figure S12 and the residuals on Figure S13. For InSAR, we plot the mean predicted line-of-sight (LOS) displacements (Figures S14–S16)

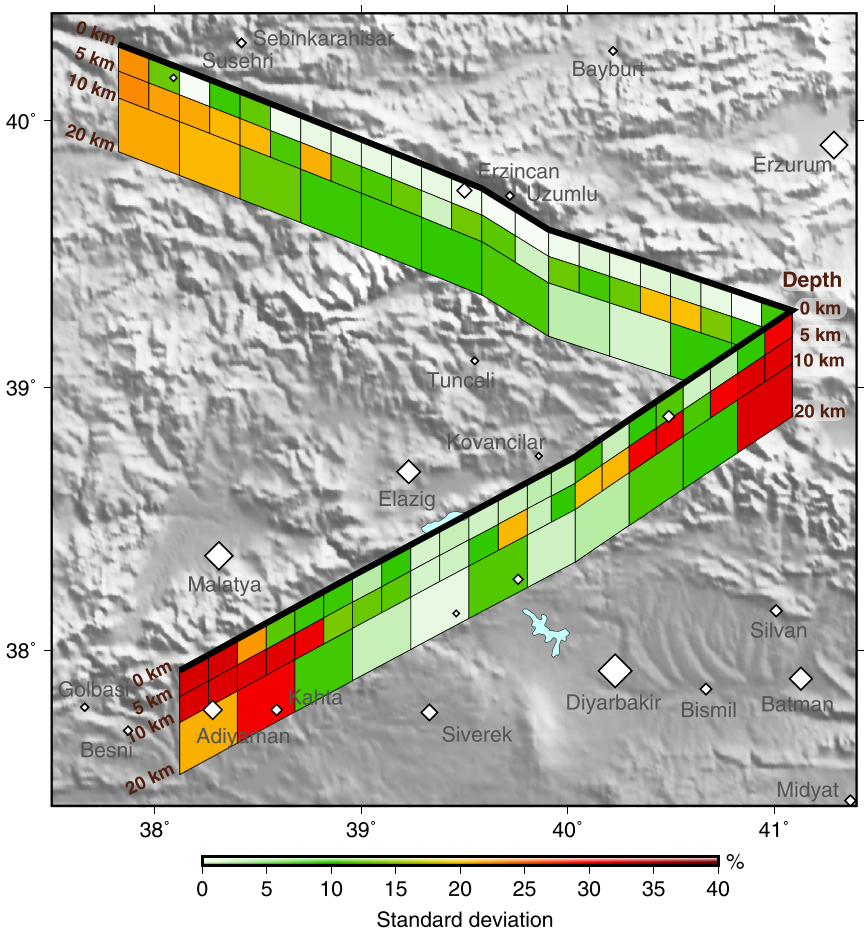

Figure 3. Standard deviation of the coupling posterior pdfs. The extreme west and—to a lesser extent—the extreme east parts of the NAF-EAF system, presenting high (>25%) standard deviations, are located outside of the InSAR tracks.

and standard deviations (Figure S17). The range of likely models that we found (Figures S10 and S11) is in very good agreement with both GPS and InSAR data. One way to quantify the relative amplitudes of residuals with respect to the observations is to calculate the ratio r of the mean of the absolute value of the residuals with the mean of the absolute value of the observations,

$$r = \frac{< |\mathbf{d} - \mathbf{d}_{\mathbf{pred}}| >}{< |\mathbf{d}| >}. \tag{6}$$

This ratio is 15.9% for T264, 36.1% for T400, 24.3% for T493, and 21.6% for GPS. We attribute these reasonably small residuals—which do not exhibit coherent pattern (Figures S13 and S17)—to nontectonic sources. Furthermore, we find that every posterior sampled model predict very similar GPS and InSAR displacements; red ellipses are hardly visible on Figure S12, and the standard deviations of the predicted InSAR LOS displacements are very small (Figure S17). This highlights the limited resolution on the coupling model: If different models predict the same observations, discriminating between them is difficult.

5. Discussion

We show focal mechanisms of $M > 4.8$ earthquakes in the studied area from the Global Centroid Moment Tensor (GCMT) catalog (Dziewonski et al., 1981; Ekström et al., 2012) for events posterior to 1976 and from a compilation of historical earthquakes (Tan et al., 2008) for earlier events (1938–1976) (Figure 2). Focal mechanisms are represented at the location of their surface projections (i.e., at depth = 0). Colors indicate the dates of the events. The largest earthquake in the studied area is the 1939 M_S 8.0 Erzincan earthquake, which initiated near Erzincan and extended over the entire NAF segment west of Erzincan represented in

Figure 2 (Barka, 1996; Stein et al., 1997). We find that almost all of this section is strongly coupled, such as the rest of the studied NAF segment east of Erzincan. This easternmost segment of the NAF presents a moderate seismicity compared to the rest of the NAF. Our interseismic slip distribution suggests that it is as prone to generate large earthquakes as the rest of the NAF and as the Erzincan rupture segment in particular. In the middle of this overall strongly coupled (>75%) fault, we identify a few low-to-moderate coupling (10–50%) patches at depths between 5 and 10 km (Figure 2). These patches are associated with standard deviations between 5% and 25%, suggesting that these uncoupled patches are robust features. Interestingly, the most uncoupled patch coincides with the main step over of this section of the NAF. Step overs are thought to act as geometrical barriers that stop earthquake ruptures (e.g., Wesnousky, 2006). Although limited to one example, our results suggest that these geometrical features may also influence—or be influenced by—the intereseismic behavior of the faults.

We find that locking on the EAF is much shallower with coupling values >50% limited to the first 5 km, consistently with previous studies (Cavalié & Jónsson, 2014). High coupling found at depth on the westernmost part of the fault is associated with standard deviations >20%, meaning that they are not reliable (Figure 3). Furthermore, we find that coupling also varies within the shallowest portion of the fault, alternating strongly coupled segments with weakly-to-moderately (0–60%) coupled ones (Figure 2). The most uncoupled shallow fault portion of the central EAF is located near Elazığ and coincides with the pull apart basin of Lake Hazar, as also observed on the Haiyuan fault (Jolivet et al., 2013). Different stress orientations around the basin could favor low coupling (Bertoluzza & Perotti, 1997; Wang et al., 2017; Van Wijk et al., 2017). This large reservoir of water may also provide the shallow part of the fault with fluids (although low resistivity associated to fluids is rather observed below 10 km depth, Türkoğlu et al., 2015) and locally weaken its mechanical friction, favoring asesimic slip. Such a behavior is observed both in laboratory and in situ (at the decametric scale) (Cappa et al., 2019). The mechanism invoked by the authors—consisting in an increase in nucleation length due to an increase in pore fluid pressure—may be at play at much larger scale here. On the other hand, the few earthquakes recorded on the EAF coincide with relatively high coupling. Before the recent Elazığ earthquake, the two largest events occurred near the localities of Bingol (M_w 6.3, 2003) and Kovancilar (M_w 6.1, 2010). The second one was followed by numerous aftershocks with magnitudes up to 5.6. All of these earthquakes occurred on >65% coupled fault portions, while fault segments with coupling <50% do not appear to have hosted $M > 4.8$ earthquakes.

According to the U.S. Geological Survey (USGS) finite-fault model (USGS, 2020), the Elazığ earthquake initiated between Elazığ and Malatya (light blue star in Figure 2) and propagated unilaterally westward (light blue contour in Figure 2). The early part coincides with a strongly locked (coupling coefficient: 100%) but narrow (13.7 × 5 km) patch. The rupture seems to have then propagated throughout moderately coupled (coupling coefficient: 50–80%) fault segments. Although the USGS model is preliminary, its contours correlate fairly well with the coupling distribution, suggesting that the rupture stopped when reaching <25% coupled fault portions (Figure 2).

The last $M > 6.6$ earthquake in the approximate region dates back to 1905 (M_S= 6.7) (Nalbant et al., 2002). This event was located west of the recent Elazığ earthquake (38.6°E, 38.1°N) (Nalbant et al., 2002) but, given location uncertainties, could have ruptured the same fault portion. We calculate, for each sampled coupling model, the accumulated moment inside the rupture contour of the Elazığ earthquake since 1905. To simplify the problem, we assume that the earthquake ruptured the entire surface of the four main subfaults inside the rupture contour and not more, that is, the three shallowest subfaults plus the westernmost intermediate-depth one (Figure 3). We obtain a pdf of the seismic moment accumulated since 1905 (Figure 4a). The pdf mean is 7.3×10^{18} N m, its standard deviation 0.8×10^{18} N m. According to the USGS solution, the seismic moment released during the Elazığ earthquake is 13.87×10^{18} N m—other solutions find even larger seismic moments (e.g., GCMT, Pousse-Beltran et al., 2020)—which is much larger than the $7.3 \pm 0.8 \times 10^{18}$ N m of moment deficit that we estimated since 1905. This seems to indicate that the recent Elazığ earthquake did not rupture the same fault portion than the 1905 earthquake. We further calculate the pdf of the time necessary to accumulate the seismic moment, which was released during the 2020 Elazığ earthquake (Figure 4b). The mean and standard deviation of the obtained pdf give a recurrence time for an Elazığ-type earthquake of 221.5 ± 26 years.

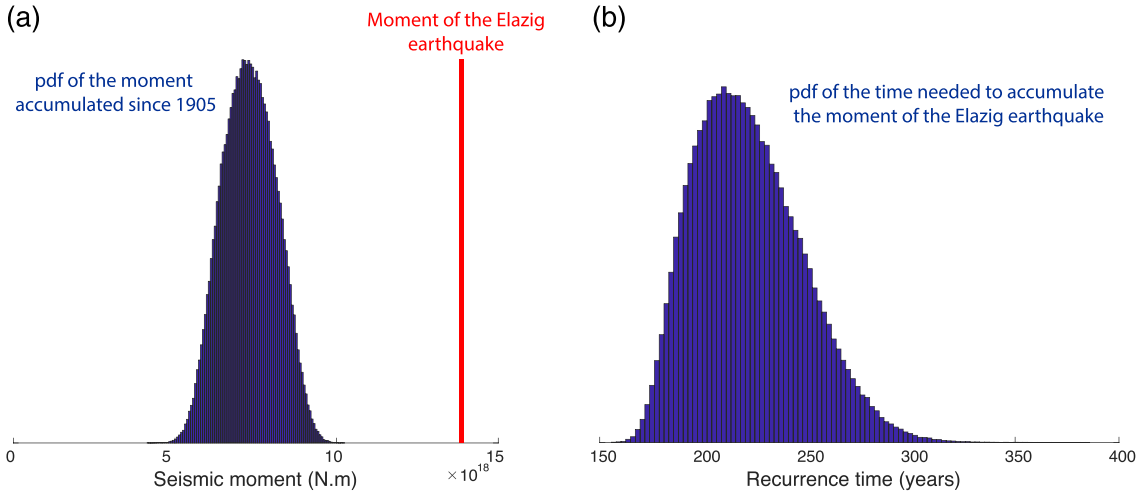

Figure 4. (a) Pdf of the accumulated seismic moment on the four patches inside the Elazığ rupture since 1905. The red vertical line indicates the seismic moment of the Elazığ earthquake according to the USGS solution (13.87×10^{18} N m). (b) Pdf of the time necessary to accumulate the seismic moment that was released during the Elazığ earthquake.

6. Conclusion

We inverted InSAR and GPS observations to image interseismic coupling along the NAF and EAF in eastern Turkey. We adopted a Bayesian sampling approach in order to estimate posterior uncertainties on the coupling distributions and on the long-term fault rate. We did not impose a precalculated plate motion but inverted for the rotation of both the Anatolian and Arabian plates with respect to Eurasia, ensuring that the inferred coupling distribution is not biased in a systematic way by an inaccurate plate motion model. We found that the NAF is strongly coupled from 0 to 20 km depth, while the EAF is weakly coupled for the most part with high (>50%) coupling values limited to the shallowest part of the fault (0 to 5 km). Furthermore, we find that coupling is heterogeneous within this shallow portion, alternating seemingly creeping sections with strongly locked patches. Comparison between our interseismic coupling distribution and the preliminary finite-fault model of the USGS for the 2020 M_w 6.8 Elazığ earthquake reveals that this event likely initiated on one of this strongly locked (coupling coefficient: 100%) fault patches and then propagated into moderately coupled fault segments (coupling coefficient: 50–80%). Overall, we estimate that the Elazığ earthquake released 221.5 (±26) years of accumulated moment, suggesting a recurrence time ranging from 200 to 250 years.

Appendix A: Rotation Matrix A

We build the rotation matrix $\mathbf{A}$ so that the motion due to the rotation of both the Anatolian and Arabian plates with respect to Eurasia equals $\mathbf{A} \cdot \mathbf{W}$, where

$$\mathbf{W} = \begin{pmatrix} \mathbf{w}^1 \\ \mathbf{w}^2 \end{pmatrix}. \tag{A1}$$

Sorting all data points located on the Eurasian plate at the beginning of $\mathbf{d}$, all data points located on the Anatolian plate in the middle and all data points located on the Arabian plate at the end, that is, writing $\mathbf{d}$ as

$$\mathbf{d} = \begin{pmatrix} \mathbf{d}_0 \\ \mathbf{d}_1 \\ \mathbf{d}_2 \end{pmatrix}, \tag{A2}$$

with $\mathbf{d}_0$, $\mathbf{d}_1$, and $\mathbf{d}_2$ data points located on the Eurasian, Anatolian, and Arabian plates respectively, we can write $\mathbf{A}$ as a block matrix

$$\mathbf{A} = \begin{pmatrix} \mathbf{0} & \mathbf{0} \\ \mathbf{A}' & \mathbf{0} \\ \mathbf{0} & \mathbf{A}' \end{pmatrix}, \tag{A3}$$

so that $\mathbf{A} \cdot \mathbf{W}$ equals $\mathbf{0}$ for data points in Eurasia, $\mathbf{A}' \cdot \mathbf{w}^1$ in Anatolia, and $\mathbf{A}' \cdot \mathbf{w}^2$ in Arabia. $\mathbf{A}'$ is a transfer matrix relating the rotation vector in Cartesian geocentric coordinates $\mathbf{W}$ to the rotation block motion at each data point. It can be expressed at the location of an InSAR pixel or GPS station of longitude λ and latitude ϕ as

$$\mathbf{A'}_{\lambda,\phi} = \begin{pmatrix} -\sin\lambda & \cos\lambda & 0 \\ -\sin\phi\cos\lambda & -\sin\phi\sin\lambda & \cos\phi \\ \cos\phi\cos\lambda & \cos\phi\sin\lambda & \sin\phi \end{pmatrix} \cdot \begin{pmatrix} 0 & z & -y \\ -z & 0 & x \\ y & -x & 0 \end{pmatrix}, \tag{A4}$$

where

$$\begin{pmatrix} x \\ y \\ z \end{pmatrix} = R_e(1 - \epsilon\sin^2\phi)^{-1/2} \begin{pmatrix} \cos\phi\cos\lambda \\ \cos\phi\sin\lambda \\ (1-\epsilon)\sin\phi \end{pmatrix}, \tag{A5}$$

with $R_e = 6{,}378.137\,\text{km}$ the Earth equatorial radius and $\epsilon = 0.00669438003$ the Earth eccentricity (Bowring, 1985).

Acknowledgments
The SAR data were provided by the European Space Agency through category1 project 6703, accessible at the following address (https://earth.esa.int/web/guest/data-access/). The inversion was performed using the AlTar software developed by Sarah Minson, Junle Jiang, Hailiang Zhang, Romain Jolivet, Zacharie Duputel, Michael Aivazis, James Beck, and Mark Simons at Caltech. We thank the Editor and Romain Jolivet and A. Ozgun Konca for thorough reviews.

References

Aktug, B., Dikmen, U., Dogru, A., & Ozener, H. (2013). Seismicity and strain accumulation around Karliova Triple Junction (Turkey). *Journal of Geodynamics*, *67*, 21–29.

Aktug, B., Ozener, H., Dogru, A., Sabuncu, A., Turgut, B., Halicioglu, K., et al. (2016). Slip rates and seismic potential on the East Anatolian Fault System using an improved GPS velocity field. *Journal of Geodynamics*, *94*, 1–12.

Ambraseys, N. (1971). Value of historical records of earthquakes. *Nature*, *232*(5310), 375–379.

Ambraseys, N. (1989). Temporary seismic quiescence: SE Turkey. *Geophysical Journal International*, *96*(2), 311–331.

Avouac, J.-P. (2015). From geodetic imaging of seismic and aseismic fault slip to dynamic modeling of the seismic cycle. *Annual Review of Earth and Planetary Sciences*, *43*, 233–271.

Barka, A. (1996). Slip distribution along the North Anatolian Fault associated with the large earthquakes of the period 1939 to 1967. *Bulletin of the Seismological Society of America*, *86*(5), 1238–1254.

Bertoluzza, L., & Perotti, C. R. (1997). A finite-element model of the stress field in strike-slip basins: Implications for the Permian tectonics of the Southern Alps (Italy). *Tectonophysics*, *280*(1-2), 185–197.

Bletery, Q., Sladen, A., Jiang, J., & Simons, M. (2016). A Bayesian source model for the 2004 great Sumatra-Andaman earthquake. *Journal of Geophysical Research: Solid Earth*, *121*, 5116–5135. https://doi.org/10.1002/2016JB012911

Bowring, B. R. (1985). The accuracy of geodetic latitude and height equations. *Survey Review*, *28*(218), 202–206.

Bürgmann, R., Kogan, M. G., Steblov, G. M., Hilley, G., Levin, V. E., & Apel, E. (2005). Interseismic coupling and asperity distribution along the Kamchatka subduction zone. *Journal of Geophysical Research*, *110*, B07405. https://doi.org/10.1029/2005JB003648

Burton, P. W., McGonigle, R., Makropoulos, K. C., & Üçer, S. B. (1984). Seismic risk in Turkey, the Aegean and the eastern Mediterranean: The occurrence of large magnitude earthquakes. *Geophysical Journal International*, *78*(2), 475–506.

Cappa, F., Scuderi, M. M., Collettini, C., Guglielmi, Y., & Avouac, J.-P. (2019). Stabilization of fault slip by fluid injection in the laboratory and in situ. *Science Advances*, *5*(3), eaau4065.

Cavalié, O., & Jónsson, S. (2014). Block-like plate movements in Eastern Anatolia observed by InSAR. *Geophysical Research Letters*, *41*, 26–31. https://doi.org/10.1002/2013GL058170

Doin, M.-P., Guillaso, S., Jolivet, R., Lasserre, C., Lodge, F., Ducret, G., & Grandin, R. (2011). Presentation of the small baseline NSBAS processing chain on a case example: The Etna deformation monitoring from 2003 to 2010 using Envisat data. In *Proceedings of the Fringe symposium*, pp. 3434–3437.

Duman, T. Y., & Emre, O. (2013). The East Anatolian Fault: Geometry, segmentation and jog characteristics. *Geological Society, London, Special Publications*, *372*(1), 495–529.

Duputel, Z., Agram, P. S., Simons, M., Minson, S. E., & Beck, J. L. (2014). Accounting for prediction uncertainty when inferring subsurface fault slip. *Geophysical Journal International*, *197*(1), 464–482.

Dziewonski, A. M., Chou, T.-A., & Woodhouse, J. H. (1981). Determination of earthquake source parameters from waveform data for studies of global and regional seismicity. *Journal of Geophysical Research*, *86*(B4), 2825–2852.

Ekström, G., Nettles, M., & Dziewoński, A. M. (2012). The global CMT project 2004–2010: Centroid-moment tensors for 13,017 earthquakes. *Physics of the Earth and Planetary Interiors*, *200*, 1–9.

England, P., Houseman, G., & Nocquet, J.-M. (2016). Constraints from GPS measurements on the dynamics of deformation in Anatolia and the Aegean. *Journal of Geophysical Research: Solid Earth*, *121*, 8888–8916.

Jackson, J., & McKenzie, D. (1988). The relationship between plate motions and seismic moment tensors, and the rates of active deformation in the Mediterranean and Middle East. *Geophysical Journal International*, *93*(1), 45–73.

Jolivet, R., Lasserre, C., Doin, M.-P., Guillaso, S., Peltzer, G., Dailu, R., et al. (2012). Shallow creep on the Haiyuan Fault (Gansu, China) revealed by SAR interferometry. *Journal of Geophysical Research: Solid Earth*, *117*, B06401. https://doi.org/10.1029/2011JB008732

Jolivet, R., Lasserre, C., Doin, M.-P., Peltzer, G., Avouac, J.-P., Sun, J., & Dailu, R. (2013). Spatio-temporal evolution of aseismic slip along the Haiyuan Fault, China: Implications for fault frictional properties. *Earth and Planetary Science Letters*, *377*, 23–33.

Jolivet, R., Simons, M., Agram, P. S., Duputel, Z., & Shen, Z.-K. (2015). Aseismic slip and seismogenic coupling along the central San Andreas Fault. *Geophysical Research Letters*, *42*, 297–306. https://doi.org/10.1002/2014GL062222

Jolivet, R., Simons, M., Duputel, Z., Olive, J.-A., Bhat, H. S., & Bletery, Q. (2020). Interseismic loading of subduction megathrust drives long term uplift in northern Chile. *Geophysical Research Letters*, *47*, e2019GL085377. https://doi.org/10.1029/2019GL085377

Jónsson, S., Zebker, H., Segall, P., & Amelung, F. (2002). Fault slip distribution of the 1999 Mw 7.1 Hector Mine, California, earthquake, estimated from satellite radar and GPS measurements. *Bulletin of the Seismological Society of America*, *92*(4), 1377–1389.

Kaneko, Y., Avouac, J.-P., & Lapusta, N. (2010). Towards inferring earthquake patterns from geodetic observations of interseismic coupling. *Nature Geoscience*, *3*(5), 363–369.

Le Pichon, X., & Kreemer, C. (2010). The Miocene-to-Present kinematic evolution of the eastern Mediterranean and Middle East and its implications for dynamics. *Annual Review of Earth and Planetary Sciences*, *38*, 323–351.
Loveless, J. P., & Meade, B. J. (2011). Spatial correlation of interseismic coupling and coseismic rupture extent of the 2011 Mw = 9.0 Tohoku-oki earthquake. *Geophysical Research Letters*, *38*, L17306. https://doi.org/10.1029/2011GL048561
Mahmoud, Y., Masson, F., Meghraoui, M., Cakir, Z., Alchalbi, A., Yavasoglu, H., et al. (2013). Kinematic study at the junction of the East Anatolian fault and the Dead Sea Fault from GPS measurements. *Journal of Geodynamics*, *67*, 30–39.
Mansinha, L., & Smylie, D. E. (1971). The displacement fields of inclined faults. *Bulletin of the Seismological Society of America*, *61*(5), 1433–1440.
Marinkovic, P., & Larsen, Y. (2013). Consequences of long-term ASAR local oscillator frequency decay—An empirical study of 10 years of data. In *Living Planet Symposium*, European Space Agency Edinburgh, Frascati.
Maurer, J., & Johnson, K. (2014). Fault coupling and potential for earthquakes on the creeping section of the central San Andreas fault. *Journal of Geophysical Research: Solid Earth*, *119*, 4414–4428. https://doi.org/10.1002/2013JB010741
Meade, B. J., & Loveless, J. P. (2009). Block modeling with connected fault-network geometries and a linear elastic coupling estimator in spherical coordinates. *Bulletin of the Seismological Society of America*, *99*(6), 3124–3139.
Metois, M., Vigny, C., & Socquet, A. (2016). Interseismic coupling, megathrust earthquakes and seismic swarms along the Chilean subduction zone (38–18 s). *Pure and Applied Geophysics*, *173*(5), 1431–1449.
Minson, S. E., Simons, M., & Beck, J. L. (2013). Bayesian inversion for finite fault earthquake source models I—Theory and algorithm. *Geophysical Journal International*, *194*(3), 1701–1726.
Moreno, M., Rosenau, M., & Oncken, O. (2010). 2010 Maule earthquake slip correlates with pre-seismic locking of Andean subduction zone. *Nature*, *467*(7312), 198–202.
Nalbant, S. S., McCloskey, J., Steacy, S., & Barka, A. A. (2002). Stress accumulation and increased seismic risk in eastern Turkey. *Earth and Planetary Science Letters*, *195*(3-4), 291–298.
Nocquet, J.-M. (2012). Present-day kinematics of the mediterranean: A comprehensive overview of GPS results. *Tectonophysics*, *579*, 220–242.
Nocquet, J.-M. (2018). Stochastic static fault slip inversion from geodetic data with non-negativity and bound constraints. *Geophysical Journal International*, *214*(1), 366–385.
Nocquet, J.-M., Calais, E., Altamimi, Z., Sillard, P., & Boucher, C. (2001). Intraplate deformation in western Europe deduced from an analysis of the international terrestrial reference frame 1997 (ITRF97) velocity field. *Journal of Geophysical Research*, *106*(B6), 11,239–11,257.
Nocquet, J.-M., Jarrin, P., Vallée, M., Mothes, P. A., Grandin, R., Rolandone, F., et al. (2017). Supercycle at the Ecuadorian subduction zone revealed after the 2016 Pedernales earthquake. *Nature Geoscience*, *10*(2), 145–149.
Okada, Y. (1985). Surface deformation due to shear and tensile faults in a half-space. *Bulletin of the seismological society of America*, *75*(4), 1135–1154.
Ozener, H., Arpat, E., Ergintav, S., Dogru, A., Cakmak, R., Turgut, B., & Dogan, U. (2010). Kinematics of the eastern part of the North Anatolian Fault Zone. *Journal of Geodynamics*, *49*(3-4), 141–150.
Pousse-Beltran, L., Nissen, E., Bergman, E. A., Cambaz, M. D., Gaudreau, E., Karasözen, E., & Tan, F. (2020). The 2020 *Mw* 6.8 Elazığ (Turkey) earthquake reveals rupture behavior of the East Anatolian Fault. *Geophysical Research Letters*, *47*, e2020GL088136. https://doi.org/10.1029/2020GL088136
Protti, M., González, V., Newman, A. V., Dixon, T. H., Schwartz, S. Y., Marshall, J. S., et al. (2014). Nicoya earthquake rupture anticipated by geodetic measurement of the locked plate interface. *Nature Geoscience*, *7*(2), 117–121.
Ragon, T., Sladen, A., Bletery, Q., Vergnolle, M., Cavalié, O., Avallone, A., et al. (2019b). Joint inversion of coseismic and early postseismic slip to optimize the information content in geodetic data: Application to the 2009 *Mw* 6.3 L'Aquila earthquake, central Italy. *Journal of Geophysical Research: Solid Earth*, *124*, 10,522–10,543. https://doi.org/10.1029/2018JB017053
Ragon, T., Sladen, A., & Simons, M. (2018). Accounting for uncertain fault geometry in earthquake source inversions—I: Theory and simplified application. *Geophysical Journal International*, *214*(2), 1174–1190.
Ragon, T., Sladen, A., & Simons, M. (2019a). Accounting for uncertain fault geometry in earthquake source inversions—II: Application to the *Mw* 6.2 Amatrice earthquake, central Italy. *Geophysical Journal International*, *218*(1), 689–707.
Reilinger, R., & McClusky, S. (2011). Nubia-Arabia-Eurasia plate motions and the dynamics of Mediterranean and Middle East tectonics. *Geophysical Journal International*, *186*(3), 971–979.
Reilinger, R., McClusky, S., Vernant, P., Lawrence, S., Ergintav, S., Cakmak, R., et al. (2006). GPS constraints on continental deformation in the Africa-Arabia-Eurasia continental collision zone and implications for the dynamics of plate interactions. *Journal of Geophysical Research*, *111*, B05411. https://doi.org/10.1029/2005JB004051
Stein, R. S., Barka, A. A., & Dieterich, J. H. (1997). Progressive failure on the north anatolian fault since 1939 by earthquake stress triggering. *Geophysical Journal International*, *128*(3), 594–604.
Sudhaus, H., & Sigurjón, J. (2009). Improved source modelling through combined use of InSAR and GPS under consideration of correlated data errors: Application to the june 2000 Kleifarvatn earthquake, Iceland. *Geophysical Journal International*, *176*(2), 389–404.
Tan, O., Tapirdamaz, M. C., & Yörük, A. (2008). The earthquake catalogues for Turkey. *Turkish Journal of Earth Sciences*, *17*(2), 405–418.
Tarantola, A., & Valette, B. (1982). Inverse problems = Quest for information. *Journal of Geophysics*, *50*(1), 159–170.
Tatar, O., Poyraz, F., Gürsoy, H., Cakir, Z., Ergintav, S., Akpınar, Z., et al. (2012). Crustal deformation and kinematics of the eastern part of the north anatolian fault zone (Turkey) from GPS measurements. *Tectonophysics*, *518*, 55–62.
Türkoğlu, E., Unsworth, M., Bulut, F., & Çağlar, I. (2015). Crustal structure of the North Anatolian and East Anatolian Fault Systems from magnetotelluric data. *Physics of the Earth and Planetary Interiors*, *241*, 1–14.
USGS (2020). Finite fault model for the 01 24 2020 *M* 6.7 earthquake, Turkey. USGS finite-fault solution.
Van Wijk, J., Axen, G., & Abera, R. (2017). Initiation, evolution and extinction of pull-apart basins: Implications for opening of the Gulf of California. *Tectonophysics*, *719*, 37–50.
Wang, H., Liu, M., Ye, J., Cao, J., & Jing, Y. (2017). Strain partitioning and stress perturbation around stepovers and bends of strike-slip faults: Numerical results. *Tectonophysics*, *721*, 211–226.
Wesnousky, S. G. (2006). Predicting the endpoints of earthquake ruptures. *Nature*, *444*(7117), 358–360.